ARTICLE

3D Printing of a Tidal Turbine Blade Using Two Methods of SLS and FFF of a Reinforced PA12 Composite: A Comparative Study

Marwane Rouway[1,3]* , Mourad Nachtane[2], Mostapha Tarfaoui[1], Sara Jamoudi Sbai[4]

[1] ENSTA Bretagne, IRDL, UMR CNRS 6027, Brest, F-29200, France

[2] S Vertical Company, Paris, F-92290, France

[3] Faculty of Sciences Aïn Chock, LPMAT Laboratory, Hassan II University, Casablanca, 20000, Morocco

[4] LIMAT Laboratory, FSBM, FSAC, Hassan II University, Casablanca, 20000, Morocco

Abstract: This study scrutinizes the thermomechanical dynamics of 3D-printed hydrofoil blades utilizing a carbon and glass bead-reinforced thermoplastic polymer. Comparative analyses underscore the pivotal role of polymer reinforcement in augmenting mechanical strength and mitigating deformation and residual stress. The investigation elucidates the expeditious and cost-efficient manufacturing potential of low-cost Fused Filament Fabrication (FFF) printers for small-scale blades, revealing exemplary mechanical performance with nominal deflection and warping in the PA12-CB/GB printed blade. A comprehensive juxtaposition between Selective Laser Sintering (SLS) and FFF printing methods favors SLS due to its isotropic properties, notwithstanding remediable warping. Emphasizing the rigorous marine environment, the study cautions against the anisotropic properties of FFF-printed blades, despite their low mechanical warping. These discernments contribute to hydrofoil design optimization through numerical analysis, shedding light on additive manufacturing's potential for small blades in renewable energy, while underscoring the imperative for further research to advance these techniques.

Keywords: 3D printing; Tidal blade; Selective laser sintering (SLS); Fused filament fabrication (FFF)

1. Introduction

Tidal energy emerges as a critical asset for coastal nations such as Morocco [1,2], offering a pathway to sustainable power by tapping into the continuous ebb and flow of tides, propelling clean and dependable electricity generation for a resilient and environmentally friendly energy landscape [3,4]. In response to escalating energy needs, the utilization of tidal turbines becomes imperative, particularly with small horizontal axis tur-

*Corresponding Author:

Marwane Rouway,

ENSTA Bretagne, IRDL, UMR CNRS 6027, Brest, F-29200, France; Faculty of Sciences Aïn Chock, LPMAT Laboratory, Hassan II University, Casablanca, 20000, Morocco;

Email: mr.rouway92@gmail.com

bines (HATT) or vertical axis turbines (VATT) designed to function in shallower and less robust currents [5–7]. The significance of these compact marine turbines lies in their cost-effectiveness, simplified manufacturing processes, and accelerated production, thereby supporting isolated communities in their quest for efficient electricity generation. The fabrication of such turbines can be achieved through advanced techniques like 3D printing or additive manufacturing (AM) [8–10], facilitating the automated construction of 3D components by layering base materials and overcoming limitations in molding fabrication methods [11,12]. Rouway et al. [13] investigate the viability of employing 3D printing technology, specifically Selective Laser Sintering (SLS), to create compact tidal turbine blades suitable for deployment in rural regions. The study focuses on utilizing specific polymers and reinforcements in the printing process, the research evaluates thermomechanical performance, revealing differences in warpage among materials. Ultimately, the findings emphasize 3D printing as a promising avenue for designing and developing efficient tidal energy systems, particularly favoring polyamide 12 reinforced with glass beads for minimal warpage. Also, in another work, Rouway et al. [14] evaluate the thermomechanical capabilities of a 3D-printed tidal turbine using Digimat-AM. They also utilize an alternative printing method, Fused Filament Fabrication (FFF). The study highlights the enhanced mechanical performance of a PEI-CB/CF blade compared to PA6-CB/CF, underscoring the 3D printing technology's potential in manufacturing small blades for green energy applications.

However, the particles are crucial for reinforcing composites, boosting their mechanical properties and overall performance [15,16]. Their strategic incorporation enhances strength, stiffness, and durability, improving the material's resistance to deformation and fracture. This reinforcement also extends to thermal and electrical conductivity, making composites versatile for diverse applications. The size and shape of particles, whether micro or nanoscale, influence the material's behavior, allowing for tailored properties. In addition, biocomposites with thermoplastic polymers and natural fibers replace non-biodegradable materials in wind turbine blades [17]. Rouway et al. [18] utilize the Mori-Tanaka approach to investigate how the elastic properties of composites are affected by the volume fraction and aspect ratio of carbon nanofillers such as CNTs and graphene. The results indicate improved performance when nanofillers are incorporated, resulting in increased Young's modulus and decreased Poisson's ratio. Additionally, distinct enhancements are noted in various orientations for polymers reinforced with CNTs and graphene nanoplatelets (GNPs).

Momeni et al. [19] found that the development of plant leaf veins follows an optimized pattern to fulfill biological functions and withstand environmental loads. Mimicking this structure, a 4D-printed wind blade exhibits improved strength, stiffness, and fatigue life. Galves et al. [20] identify the hexagonal infill pattern as effective in tidal turbine blade construction, Providing a substitute for the traditional shell-spar framework. Ramírez-Elías et al. [21] analyzed 3D-printed wind turbine ribs using PLA and CF-PLA materials, revealing higher compression strength with built-in holes. Arivalagan et al. [22] innovated a micro wind turbine blade utilizing 3D printing technology and PLA material, designed specifically for low-wind-speed scenarios. Arivalagan et al. [23] presented a printing technique using low-energy electron beam curing to enhance lightning protection on GFRP wind turbine blades. Findings indicated that the incorporation of a printed carbon fiber mesh successfully mitigated damage caused by simulated lightning strikes, ensuring the maintenance of structural integrity with a residual strength of 90.1%. Ming et al. [24] explored the application of a 3D printed continuous carbon fiber (CCF)/epoxy mesh with self-heating properties for deicing purposes. The printed mesh exhibited stable resistance after undergoing hot-cold cycles and demonstrated an 85% reduction in deicing time compared to glass fiber-reinforced composites. In a separate investigation, Kim et al. [25] investigated the incorporation of an optical fiber sensor into a turbine blade made of 3D-printed Ni-alloy. This allowed accurate temperature monitoring up to 500°C using directed energy deposition (DED) printing. The adoption of a strategy involving "line-by-line printing and stop" effectively reduced thermal energy accumulation, demonstrating the feasibility of monitoring high temperatures in complex metal structures.

Recycled composite waste transforms into 3D printing filaments, presenting an environmentally friendly alternative. This sustainable approach aims to diminish the ecological footprint and encourage circular practices in manufacturing, thereby supporting the conservation of resources [26]. The utilization of repurposed composites contributes to the development of inventive and functional products. In addressing the challenge of wind turbine blade composite waste, Rahimizadeh et al. [27] propose a recycling solution utilizing 3D printing technology. According to their study, incorporating recycled material into polylactic acid (PLA)

filaments results in increased specific tensile strength and modulus when compared to PLA samples without recyclate. The validity of this recycling method was confirmed through thermogravimetric analysis and micro-computed tomography, suggesting the potential to create environmentally friendly materials with enhanced mechanical properties. Furthermore, Rahimizadeh et al. [28] present a recycling approach that employs mechanical grinding and 3D printing to improve the mechanical characteristics of 3D printed parts by integrating reinforcement fibers sourced from decommissioned turbine blades. The outcomes indicate a 16% enhancement in elastic modulus and a 10% elevation in ultimate strength, underscoring the viability of environmentally sustainable utilization of materials from retired wind turbine blades. Meanwhile, Tahir et al. [29] concentrate on the effect of recycled fiber categories on the tensile behaviors of 3D-printed PLA specimens derived from wind turbine blade waste, revealing that ground fibers exhibit higher ultimate tensile strength, while pyrolyzed fibers display elevated stiffness values. The alignment of micromechanical models with experimental results offers valuable insights into the effects of recycled fibers on material properties.

2. Materials and Methods

2.1 Materials

The Fused Filament Fabrication (FFF) and Selective Laser Sintering (SLS) printing methods make use of PA12 thermoplastic polymer, chosen for its high strength and recyclability. These technologies are employed for printing tidal turbines, utilizing both unreinforced and reinforced PA12 polymers with carbon (CB) and glass (GB) beads. Figure 1 illustrates the thermomechanical properties of PA12 concerning temperature, including Young's modulus, density, specific heat capacity, and thermal expansion coefficient (CTE). Refer to Table 1 for further details. Additionally, Table 2 presents the thermomechanical properties of CB/GB fillers.

Table 1. Thermomechanical properties of PA12 polymer.

Properties	Values
Glass transition temperature T_g (°C)	49
Melting temperature T_m (°C)	180
Thermal conductivity (W/Kg.K)	0.3
Poisson ratio v	0.39

Table 2. Thermomechanical properties of CB/GB fillers.

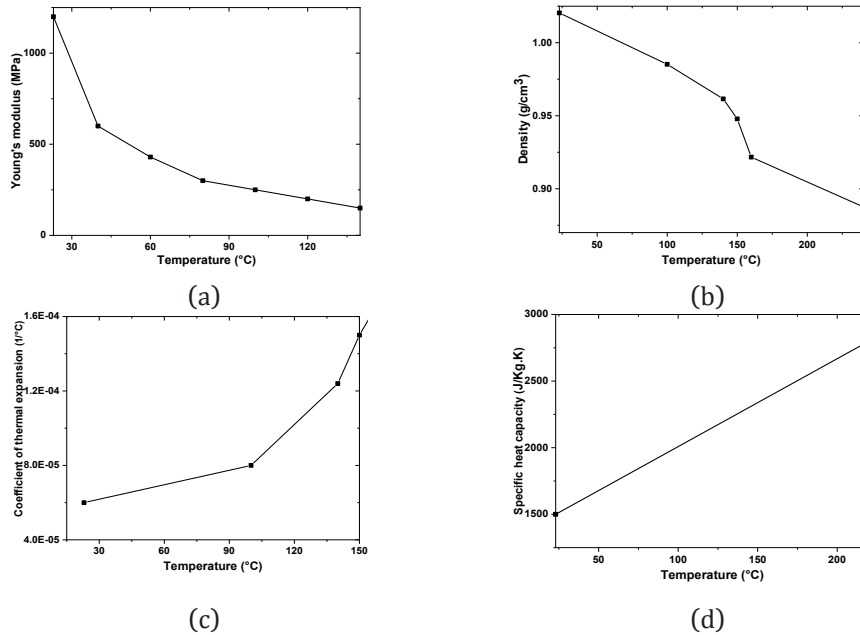| Properties	Carbon beads (CB)	Glass beads (GB)
Density (g/cm^3)	1.78	2.54
Diameter (mm)	0.05	0.05
Young's modulus ($×10^3$ MPa)	230	72
Poisson's ratio	0.2	0.22
Thermal conductivity (W/m.K)	1.7	0.8
Specific heat capacity (J/Kg.K)	720	753
Coefficient of thermal expansion ($×10^{-6}$ 1/°C)	2	6

(a)

(b)

(c)

(d)

Figure 1. Thermomechanical properties of thermoplastic polymers.

2.2 Methods

Aerodynamics and Geometry of the Hydrofoil

When a hydrofoil comes into contact with a water current, the hydrofoil's structure is influenced by the speed, creating a pressure difference between its upper (extrados) and lower (intrados) surfaces, as illustrated in Figure 2a. Typically, hydrofoils are designed to produce increased pressure, resulting in a force perpendicular to the relative velocity known as the lift force (*L*). At the same time, there is a force acting parallel to the direction of the relative velocity, caused by the hydrofoil's opposition to fluid movement, known as the drag force (*D*). These forces are commonly transformed into dimensionless parameters denoted as the lift coefficient (C_L) and drag coefficient (C_D), as articulated in Equation (10).

$$C_L = \frac{L}{0.5\rho V^2 A} \text{ and } C_D = \frac{D}{0.5\rho V^2 A}$$

(1)

where ρ represents the density of seawater measured in (kg/m^3), *V* denotes the varying velocity of ocean currents expressed in (m/s), *A* represents the area of the hydrofoil blade measured in (m^2), and *L* and *D* refer to the lift and drag forces, respectively, measured in (N).

The hydrofoil utilized in this investigation was created by the IRDL laboratory team at ENSTA Bretagne. It involved modifying the configuration of a high-lift hydrofoil designed for low Reynolds number (*Re*=2.10^6) and possessing high lift capacity, similar to the WORTMANN (FX74-CL5-140). The refined hydrofoil, named NTS1020 (Nachtane-Tarfaoui-Saifaoui-1020), demonstrated optimal suitability for a marine current turbine as depicted in Figure 3. Noteworthy adjustments included a 10% increase in curvature and a 20% increase in thickness, as illustrated in Figure 2. Detailed dimensions of the hydrofoil are presented in Figure 5. The NTS1020 hydrofoil exhibited superior hydrodynamic performance, featuring a lower drag coefficient (C_D) and a higher lift coefficient (C_L) when compared to the reference hydrofoil (FX74-CL5-140). Notably, it showcased enhanced thickness in comparison to the FX74-CL5-140, contributing to the improved structural strength of the blade, as evident in Figure 4 and Figure 5. The profile, designed for printing purposes, possesses significant properties that necessitate experimental testing to comprehend the impact of printing on aerodynamic coefficients.
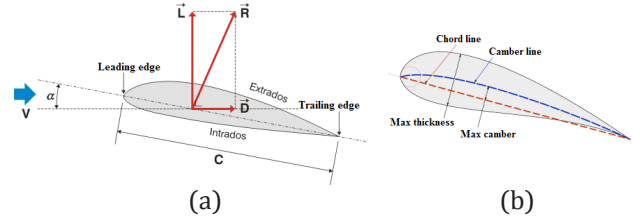

(a)   (b)

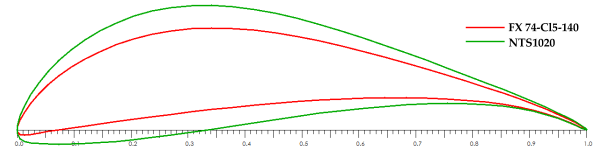**Figure 2.** Characteristic of the hydrodynamic profile (a). Thickness and curvature of the profile (b).

Source: [30].

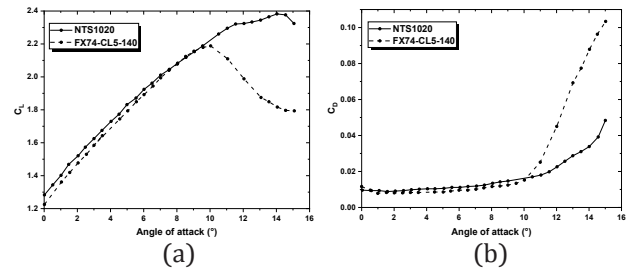**Figure 3**. The geometry parameters of the NTS1020 hydrofoil compared to the FX74-CL5-140.

(a)   (b)

Figure 4. Aerodynamic lift coefficients C_L (a) and drag coefficients C_D (b) as a function of angles of attack.

Selective Laser Sintering SLS process

The Selective Laser Sintering (SLS) process involves the fusion of thin layers of powder, typically 0.1 mm in thickness, distributed evenly across the construction area using a powder leveling roller. The part is fabricated within a sealed chamber filled with nitrogen gas to minimize oxidation and deterioration of the powder material. The powder on the build platform is maintained at an elevated temperature just below the melting point and/or the glass transition temperature T_g of the powder [31]. Infrared heaters are strategically positioned above the build platform to maintain a high temperature around the forming part and above the feed cartridges to preheat the powder before spreading it across the construction area. At times, resistive heating elements placed around the platform are utilized to heat the build platform. This preliminary heating of the powder and maintaining a consistent high temperature on the platform are essential to decrease the laser energy required for the process. The preheating phase reduces the laser energy needed for melting and serves to prevent distortion of the part during fabrication caused by uneven thermal expansion and
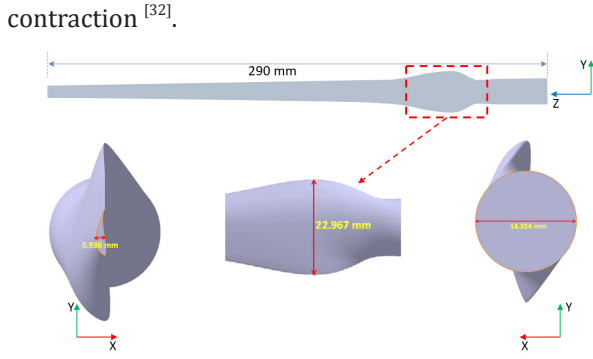
contraction [32].

Figure 5. Geometric dimension of the blade.

After the formation and preheating of an appropriate powder layer, a focused CO_2 laser beam is employed to irradiate the powder bed. The beam is manipulated by galvanometers to thermally fuse the material, creating a cross-sectional slice. Following the completion of each layer, the build platform descends by a thickness corresponding to one layer, and a fresh layer of powder is applied and distributed employing a counter-rotating roller. The laser proceeds to survey the cross-sectional area of the following slice. This sequence repeats until the entire component is constructed, as depicted in Figure 6. A cooling phase is typically necessary to ensure uniform cooling of the parts to a temperature suitable for handling and exposure to ambient conditions. Premature exposure of components and/or the powder bed to room temperature may cause powder deterioration in the presence of oxygen, leading to uneven thermal contraction and consequent distortion of the parts. Ultimately, the components are extracted from the powder bed, cleaned, and subjected to finishing processes. The primary limitation of the SLS method stems from its elevated operating temperatures, which constrain its suitability for biodegradable materials [33].

The initial step in the 3D printing procedure involves creating the geometric design of a component using Computer-Aided Design (CAD) software. Subsequently, the design file undergoes conversion into the Stereolithography (STL) file format, a widely employed format compatible with various Additive Manufacturing (AM) machines. The design is subsequently sliced into thin layers by slicing software. Information about the part, such as layer thickness, toolpath, part orientation, material type, layer count, infill density, and pattern type, is required. This information is prepared in the slicing software and incorporated into the STL file. The file is then sent to the 3D printing machine and used as a command during the fabrication of the part. The additive manufacturing process has been summarized in eight steps, as illustrated in Figure 7 [34].
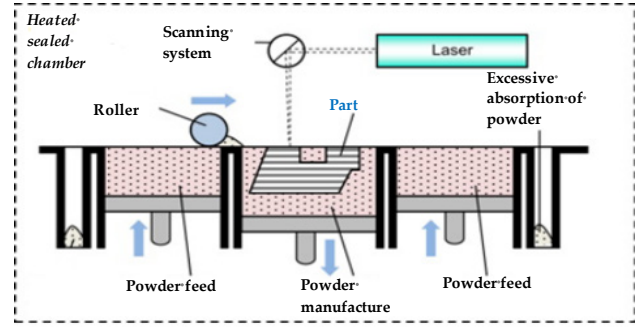

Figure 6. Diagram of the selective laser sintering (SLS) process.
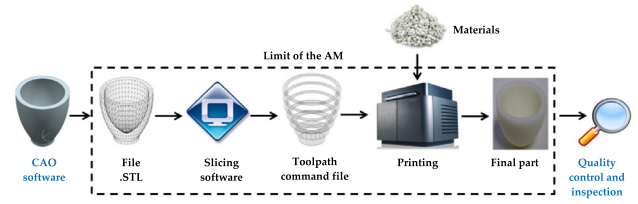
Source: [35].

Figure 7. The additive manufacturing process chain.

Source: [34].

i. Mathematical Models for SLS

The fundamental equations describing the mechanical and thermal behavior of materials in liquid form during polymer melting, as well as the circulation of hot air in the printing chamber, are defined by the conservation laws recognized in the principles of mass, energy, and momentum conservation [36]. These equations are summarized as follows:

- **The continuity equation:**

$$\frac{\partial \rho}{\partial t} + \nabla(\rho \mathbf{v}) = 0$$

(2)

- **The momentum equation:**

$$\frac{\partial(\rho \mathbf{v})}{\partial t} + \nabla(\rho \mathbf{v} \times \mathbf{v}) - \nabla(\mu_{eff} \nabla \mathbf{v}) = -\nabla p + \nabla(\mu_{eff} \nabla \mathbf{v})^T + S$$

(3)

- **The energy equation:**

$$\frac{\partial(\rho h)}{\partial t} - \frac{\partial p}{\partial t} + \nabla(\rho \mathbf{v} h) = \nabla\left[\left(\mu + \frac{\mu_t}{\sigma_t}\right)\nabla h\right] - S_h$$

(4)

with p being the pressure in (Pa), S representing the energy source, S_h being the volumetric heat flux in (kJ/m^3s), t denoting time in (h), and v indicating velocity

in (m/s). Additionally, μ, μ_{eff}, and μ_t stand for viscosity, effective viscosity, and turbulent viscosity in $(N.s/m^2)$, and h represents enthalpy in (J/kg). The notation ∇ signifies the divergence operator: $\nabla.u = \text{div u}$

The velocity gradient is simply a matrix of first-order spatial derivatives:

$v = [v_x, v_y, v_z]$:

$$\nabla \mathbf{v} = \begin{bmatrix} \dfrac{\partial v_x}{\partial x} & \dfrac{\partial v_x}{\partial y} & \dfrac{\partial v_x}{\partial z} \\ \dfrac{\partial v_y}{\partial x} & \dfrac{\partial v_y}{\partial y} & \dfrac{\partial v_y}{\partial z} \\ \dfrac{\partial v_z}{\partial x} & \dfrac{\partial v_z}{\partial y} & \dfrac{\partial v_z}{\partial z} \end{bmatrix}$$

(5)

In the SLS additive manufacturing process, a heated powder layer is subjected to selective laser exposure, enabling the creation of three-dimensional solid components made of either polymer or metal. The key physical phenomena linked with the SLS approach involve heat transfer and powder sintering. The comprehensive modeling of the SLS procedure encompasses optical, thermal, and sintering aspects.

a. Optical Model

The manifestation of optical traits is evident as the laser beam engages with the surface of the powder bed. The optical framework takes into account different phenomena, including reflection, transmission, and absorption. In the SLS workstation, a resilient CO_2 laser is utilized as a source of thermal energy to initiate selective melting. Generally, laser energy is characterized by a significant thermal flux concentrated within a confined area. The pattern of laser intensity (I) across the beam diameter follows a Gaussian correlation [37]:

$$I(t,w) = (1-R)I_0 \exp\left(-\frac{2r^2}{w^2}\right)$$

with:

$$I_0 = \frac{2P}{\pi w^2}$$

(6)

The reflectivity of the material surface is denoted by R. The maximum intensity of the beam, represented by I_0, is determined by the laser power (P) and the radius (w) of the laser intensity profile. The variable r signifies the radial distance measured from the central point of the laser beam.

b. Thermal Conductivity Model

The effective thermal conductivity k_e within the region is influenced by not just the temperature of the powder bed but also by various factors such as the thermal conductivity of the solid material (k_s), the thermal conductivity of the air (k_g), and the porosity (ϕ). Yagi-Kuni [38] has introduced a thermal conductivity calculation model that distinguishes between two temperature conditions: low and high temperatures. Under low-temperature conditions, thermal conductivity is predominantly affected by convection. Conversely, at high temperatures, the contribution of radiation to heat transfer becomes significant, consequently influencing thermal conductivity.

$$k_e = \begin{cases} k_s(1-\phi)/(1+\varphi k_s/k_g) & \text{for } T \le 673°K \\ (1-\phi)/\left[1/k_s + \varphi/\left(k_g + \varphi D_p h_{rs}\right)\right] + \phi D_p h_{rv} & \text{for } T > 673°K \end{cases}$$

$(W/m.°K)$

with:

$$\varphi = 0.02 \times 10^{2(\phi-3)}$$

(7)

The parameter φ is influenced by the material's porosity, represented by ϕ, and D_p denotes the diameter of the powder grains. The heat transfer coefficients related to radiation, h_{rs} and h_{rv}, apply to the powder grain's surface and the gaps between them, respectively.

c. Thermal Model

Thermal performance pertains to the mechanisms of heat transfer resulting from the infiltration of laser light into the powder bed. The thermal model encompasses phenomena such as conduction, convection, and radiation. In the SLS process, which focuses solely on an exterior heat flux (q) per unit incoming area into the body, the heat transfer characteristics can be elucidated using the fundamental equation of energy balance:

$$\int_\Omega \rho \overset{g}{U} d\Omega = \int_S q dS$$

(8)

where ρ represents the effective density of the powder bed, while Ω denotes the volume occupied by the powder material with a surface area S. Equation (7) incorporates input parameters such as density, specific heat and thermal conductivity. It assumes an initial distribution of uniform temperature across the powder bed before the sintering process, set equivalent to the preheating temperature. The equation of heat transfer for the powder considers both radiation and convection mechanisms:

$$-k_e \frac{\partial T}{\partial z} = h\left(T_a - T\right) + \varepsilon_R \sigma_B \left(T_a^{\;4} - T^4\right)$$

(9)

where T represents the powder bed temperature, T_a denotes the external environment temperature, h stands for the convective coefficient heat, ε_R signifies the material's surface emissivity, and σ_B represents the Stefan-Boltzmann constant.

d. Sintering Model

The sintering behavior typically pertains to the transformation of a material from a powdered state to a solid state during the sintering process, involving changes in the local powder density ρ [38]. The changing density of material over time is explained by the following differential equation that is dependent on time:

$$\frac{d\rho}{dt} = \left(\rho^{\max} - \rho\right) A \exp\left(-\frac{E}{RT}\right)$$

(10)

The symbol ρ^{max} represents the density of the solidified substance. The activation energy, denoted as E, is adjusted to a suitable value to ensure favorable sintering kinetics, taking into account the established parameters of the process. A represents the pre-exponential factor, which is unique to each material and is measured in units of s^{-1}.

ii. SLS Process Parameters

The manuscript employs Digimat-AM software, which offers thermomechanical analysis capabilities, for conducting numerical simulations pertinent to 3D printing. This software serves as a valuable tool for both printer manufacturers and end-users by facilitating the detection of manufacturing challenges. Through numerical simulation, hundreds of printing possibilities can be tested and studied prior to final blade production. Additionally, Digimat-AM autonomously computes the characteristics of reinforced polymers, leveraging the distinct thermomechanical attributes of polymers and filler particles/fibers via the Mori-Tanaka homogenization method. This approach streamlines the assessment and enhancement of 3D printed components, optimizing their performance and structural integrity.

The process of 3D printing, also known as Additive Manufacturing (AM), initiates with the creation of the hydrofoil profile-oriented blade structure through CAD design tools like CATIA. This investigation utilizes Digimat-AM to simulate diverse material setups, forecasting and evaluating the functionality of the manufactured components. Figure 8 outlines the sequential stages involved in digitally printing a tidal turbine blade. It is important to highlight that the success of 3D printing is contingent upon various factors including the specific process employed, the material used, thermomechanical constraints, and more. According to the scheme presented in Figure 8, the first step involves defining the geometry of the blade to be printed in the form of an STL file and the thermomechanical properties of polymer-based composites and particles. The thermoplastic polymer used is polyamide 12 (PA12) due to its biocompatibility for tidal applications. Afterwards, the blade's structure is modeled using the voxel technique for sequential printing. The printing procedure involves various variables, including tool path and specific inputs, to outline the manufacturing steps. Subsequently, the parameters of the additive manufacturing (AM) process are converted into a thermomechanical simulation, considering heat transfer mechanisms within the printing device. Following a finite element simulation, the outcomes are presented in the form of residual stresses using von Mises, temperature fields, deflection, and mechanical warping of the printed blade. The Selective Laser Sintering (SLS) process involves sintering plastic powder within the solid part. In this process, a laser source selectively melts the powder by scanning cross-sectional areas derived from the numerical model of the blade. Subsequent layers undergo sintering after the deposition of new powder, and this iterative process continues until the entire blade is printed. The parameters for the SLS printing process applied to the blade are detailed in Table 3, outlining the printing process's boundary conditions. These parameters are carefully determined and optimized to minimize warping and mechanical stresses. The blade is printed in a vertical orientation and is divided into three zones: the lower cylindrical zone (A), the twisted central zone (B), and the upper fine zone (C), as depicted in Figure 5. The blade experiences two stages during manufacturing—printing and cooling. Its thermomechanical behavior and warping are analyzed using Digimat-AM.

Table 3. SLS printing parameters for the blade.

Parameters	Values
Chamber temperature (°C)	330
Laser power (W)	48
Convection coefficient (W/m^2.°C)	15
Scanner spacing (mm)	0.15
Recovery time (s)	10
Scanning speed (mm/s)	12500
Beam diameter (mm)	0.5

Fused Filament Fabrication FFF

The Fused Filament Fabrication (FFF) process operates by extruding a thermoplastic polymer above its melting point. This method, widely employed due to its simplicity, affordability, and minimal waste, produces printed parts typically composed of pure thermoplastic material. Consequently, these parts exhibit characteristics such as low strength, rigidity, and compromised structural performance [39]. Mechanical properties of the fabricated components vary based on factors like filament material, extrusion process, and design parameters. The key components of an FFF printer include the heated extrusion head, nozzle, and build platform, with movement capabilities in three directions (*x*,*y*,*z*) and the option for heating. The extrusion head's movement in the (*x*,*y*), (*x*,*z*), or (*y*,*z*) directions influences print resolution (see Figure 9). Nozzle diameters range from 250 μm to 400 μm, while filament diameters typically measure 1.75 mm. The thermoplastic filament, heated just above its melting point, is fed into the extrusion head and then extruded through the nozzle onto the build platform. Step by step, this sequence recurs until the 3D model is finished. Solidification of the extruded filament occurs through cooling, ensuring precise control over pore size, shape, and homogeneity. The extruder comprises a cold end for filament intake and a hot end, typically aluminum, heated by a heating cartridge. This heating element melts the filament as it moves through the thermal tube toward the nozzle. A forced air cooling system, integrated with the print head, prevents excessive heat in extruder sections requiring lower temperatures.
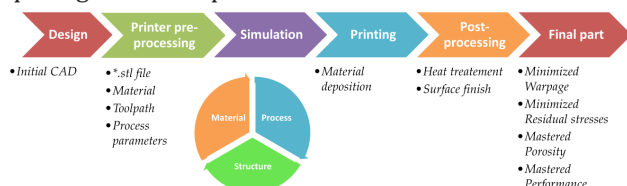

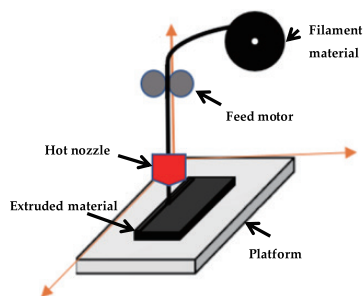**Figure 8**. 3D Printing flowchart for the hydroturbine by Digimat-AM.

Figure 9. The Fused Filament Fabrication (FFF) manufacturing method.

Recent progress in additive manufacturing includes integrating strengthening substances into thermoplastic polymers to augment the mechanical characteristics of printed components. This enhancement involves introducing reinforcing fibers, like carbon and glass fibers, into polymer filaments. In a research conducted by Shofner et al. [40], an ABS matrix was employed to create nanofiber-reinforced composites through the FDM method. The filament comprised single-walled carbon nanotubes and ABS plastic. Following the filament's creation, a 40% improvement in tensile strength and a 60% increase in Young's modulus were observed in the printed parts.

This section elucidates the origin of distortion in printed components during the FFF printing process. When a heated thermoplastic layer is laid down, it undergoes a cooling and solidification process, leading to contraction. This layer is applied to a preceding layer that has already undergone cooling and contraction. The newly deposited layer adheres to a colder layer, and due to the differing rates of thermal expansion between the layers, they contract unequally until reaching thermal equilibrium. Consequently, the upper layer contracts in relation to the lower layer, generating residual thermal stress within the plastic layers [41]. The lower section of the upper layer experiences tension, while the upper part of the lower layer undergoes compression, resulting in shear stress at the layer interface. If these stresses surpass the mechanical strength of the component and the adhesion of the build plate, deformation occurs, as depicted in Figure 10a. Without proper protection against shrinkage, thermal contraction induces warping [42]. Alternatively, if the part is constrained by build plate adhesion, cooling leads to the development of thermal stresses rather than mechanical thermal deformation, as illustrated in Figure 10b.

The challenge of warping in 3D printing extends beyond mere avoidance of visible defects like edge cracking or deformation. High residual stresses resulting from warping can significantly compromise the strength of printed objects, as stressed interlayer bonding may break under mechanical load. Abrupt temperature changes during printing exacerbate stress concentration, leading to potential layer separation and altered fracture envelopes [9]. Addressing warping begins with filament selection, as filament properties interact with printing conditions to induce warping [43]. Materials with higher glass transition temperatures, such as ABS and polycarbonate, require elevated chamber temperatures to minimize thermal shrinkage and deformation. Professional FFF printers with heated

build chambers offer an effective solution, maintaining temperatures below the material's glass transition temperature to reduce shrinkage and optimize part strength [44]. Specific chamber temperatures within the filament's creep zone are crucial, ensuring minimal warping and maximal part strength. For example, ABS performs well in an 85 °C chamber, while PLA benefits from a 35 °C chamber with adequate airflow for cooling during printing [44].
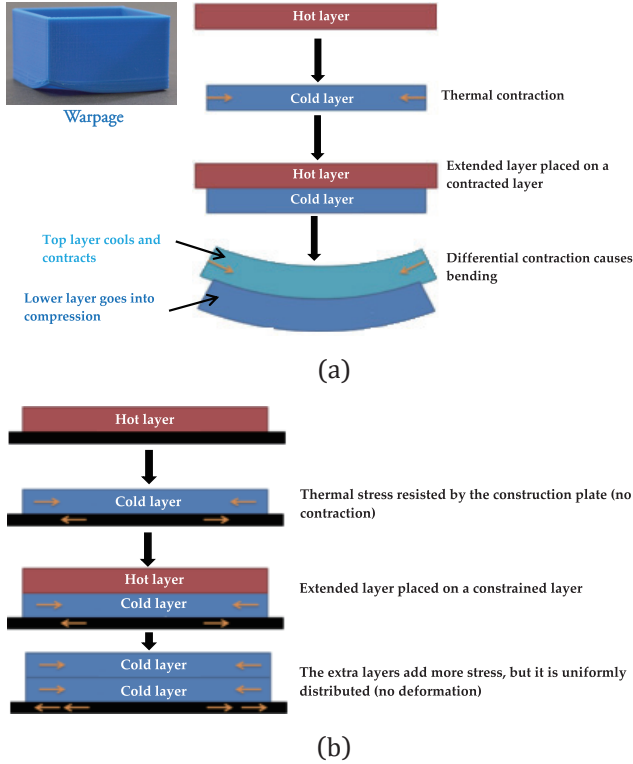

(a)

(b)

Figure 10. The deposited layers during printing. Poor adhesion (a) and adequate adhesion (b).

Filament selection for 3D printing is often driven by desired material properties, while integrating heated build chambers into printers presents ongoing challenges due to factors like patents and costs. Two main strategies address warping: adhesion surfaces, which mechanically secure prints but may not prevent delamination, and heated build plates, which enhance adhesion and minimize thermal shrinkage. However, maintaining an excessively high build plate temperature can exacerbate warping by softening the lower part of the print beyond its ability to resist stresses from cooler layers above. Temperature control is crucial, with heated build plate temperatures typically slightly higher than chamber temperatures due to measurement considerations and layer cooling during printing.i. Mathematical Models for FFF.

a. Mechanical Analysis

To utilize the finite element model in forecasting the thermo-mechanical characteristics of printed components, it becomes essential to articulate the constitutive equation dictating their mechanical response. The mechanical behavior of polymer composites under linear elasticity adheres to Hooke's law, which delineates the correlation between stress and strain in a subsequent manner:

$$
\begin{pmatrix} \varepsilon_{11} \\ \varepsilon_{22} \\ \varepsilon_{33} \\ \gamma_{12} \\ \gamma_{23} \\ \gamma_{31} \end{pmatrix} = \begin{pmatrix} S_{11} & S_{12} & S_{13} & S_{14} & S_{15} & S_{16} \\ & S_{22} & S_{23} & S_{24} & S_{25} & S_{26} \\ & & S_{33} & S_{34} & S_{35} & S_{36} \\ & & & S_{44} & S_{45} & S_{46} \\ & sym. & & & S_{55} & S_{56} \\ & & & & & S_{66} \end{pmatrix} \cdot \begin{pmatrix} \sigma_{11} \\ \sigma_{22} \\ \sigma_{33} \\ \tau_{12} \\ \tau_{23} \\ \tau_{31} \end{pmatrix}
$$

(11)

where ε is the normal strain, γ is the shear strain, τ is the shear stress, and σ is the normal stress. Also, Equation (11) can be rewritten in tensor notation as follows:

$$
\left\langle \varepsilon_{ij} \right\rangle = S : \left\{ \sigma_{ij} \right\}
$$

(12)

No presumptions have been employed thus far, except elasticity. Therefore, Equation (11) remains applicable to any anisotropic domain lacking symmetry elements.

For a material characterized as orthotropic, denoting a substance with three planes of symmetry that are mutually perpendicular, Equation (11) transforms in the following manner:

$$
\begin{pmatrix} \varepsilon_{11} \\ \varepsilon_{22} \\ \varepsilon_{33} \\ \gamma_{12} \\ \gamma_{23} \\ \gamma_{31} \end{pmatrix} = \begin{pmatrix} S_{11} & S_{12} & S_{13} & 0 & 0 & 0 \\ & S_{22} & S_{23} & 0 & 0 & 0 \\ & & S_{33} & 0 & 0 & 0 \\ & & & S_{44} & 0 & 0 \\ & sym. & & & S_{55} & 0 \\ & & & & & S_{66} \end{pmatrix} \cdot \begin{pmatrix} \sigma_{11} \\ \sigma_{22} \\ \sigma_{33} \\ \tau_{12} \\ \tau_{23} \\ \tau_{31} \end{pmatrix}
$$

(13)

Equation (13) can be condensed with respect to the nine variables by taking into account the elastic constants, including Young's modulus (E_{ij}), Poisson's ratio (v_{ij}), and shear modulus (G_{ij}), in the following manner:

$$
\begin{pmatrix} \varepsilon_{11} \\ \varepsilon_{22} \\ \varepsilon_{33} \\ \gamma_{12} \\ \gamma_{23} \\ \gamma_{31} \end{pmatrix} = \begin{pmatrix} 1/E_{11} & -v_{12}/E_{11} & -v_{13}/E_{11} & 0 & 0 & 0 \\ & 1/E_{22} & -v_{23}/E_{22} & 0 & 0 & 0 \\ & & 1/E_{33} & 0 & 0 & 0 \\ & & & 1/G_{23} & 0 & 0 \\ & sym. & & & 1/G_{13} & 0 \\ & & & & & 1/G_{12} \end{pmatrix} \cdot \begin{pmatrix} \sigma_{11} \\ \sigma_{22} \\ \sigma_{33} \\ \tau_{12} \\ \tau_{23} \\ \tau_{31} \end{pmatrix}
$$

(14)

with: (20)

$$E_{11} = \frac{\sigma_{11}}{\varepsilon_{11}} \ , \ E_{22} = \frac{\sigma_{22}}{\varepsilon_{22}} \ , \ E_{33} = \frac{\sigma_{33}}{\varepsilon_{33}}$$

$$v_{12} = -\frac{\varepsilon_{22}}{\varepsilon_{11}} \ , \ v_{13} = -\frac{\varepsilon_{33}}{\varepsilon_{11}} \ , \ v_{23} = -\frac{\varepsilon_{33}}{\varepsilon_{22}}$$

(15)

And we have substituted:

$$S_{11} = \frac{1}{E_{11}} \ , \ S_{12} = \frac{-v_{12}}{E_{11}} = \frac{-v_{21}}{E_{22}} \ , \ S_{13} = \frac{-v_{13}}{E_{11}} = \frac{-v_{31}}{E_{33}}$$

$$S_{22} = \frac{1}{E_{22}} \ , \ S_{23} = \frac{-v_{21}}{E_{22}} = \frac{-v_{12}}{E_{11}} \ , \ S_{33} = \frac{1}{E_{33}}$$

$$S_{44} = \frac{1}{G_{23}} \ , \ S_{55} = \frac{1}{G_{13}} \ , \ S_{66} = \frac{1}{G_{12}}$$

(16)

By rephrasing Equation (14), the stress matrix can be represented using the tensorial product of the stiffness matrix C and the strain tensor ε_{ij}:

$$\langle \sigma_{ij} \rangle = C : \{ \varepsilon_{ij} \}$$

(17)

The compliance matrix S is derived by inversely transforming the stiffness matrix C, resulting in the subsequent matrix:

$$\begin{pmatrix} \sigma_{11} \\ \sigma_{22} \\ \sigma_{33} \\ \tau_{12} \\ \tau_{23} \\ \tau_{31} \end{pmatrix} = \begin{pmatrix} C_{11} & C_{12} & C_{13} & 0 & 0 & 0 \\ & C_{22} & C_{23} & 0 & 0 & 0 \\ & & C_{33} & 0 & 0 & 0 \\ & & & C_{44} & 0 & 0 \\ & sym. & & & C_{55} & 0 \\ & & & & & C_{66} \end{pmatrix} \cdot \begin{pmatrix} \varepsilon_{11} \\ \varepsilon_{22} \\ \varepsilon_{33} \\ \gamma_{12} \\ \gamma_{23} \\ \gamma_{31} \end{pmatrix}$$

(18)

with:

$$C_{11} = \frac{(S_{22}S_{33} - S_{23}{}^2)}{S} \ , \ C_{22} = \frac{(S_{11}S_{33} - S_{13}{}^2)}{S} \ , \ C_{33} = \frac{(S_{11}S_{22} - S_{12}{}^2)}{S}$$

$$C_{12} = \frac{(S_{23}S_{13} - S_{12}S_{33})}{S} \ , \ C_{13} = \frac{(S_{12}S_{23} - S_{22}S_{13})}{S} \ , \ C_{23} = \frac{(S_{12}S_{13} - S_{11}S_{23})}{S}$$

$$C_{44} = \frac{1}{S_{44}}, C_{55} = \frac{1}{S_{55}}, C_{66} = \frac{1}{S_{66}}$$

$$S = S_{11}S_{22}S_{33} + 2S_{12}S_{23}S_{13} - S_{13}{}^2 S_{22} - S_{23}{}^2 S_{11} - S_{13}{}^2 S_{33}$$

(19)

The determination of Young's modulus and Poisson's ratio can be achieved in the following manner:

$$E_{11} = \frac{\sigma_{11}}{\varepsilon_{11}} \ , \ E_{22} = E_{33} = \frac{\sigma_{22}}{\varepsilon_{22}}$$

$$v_{12} = v_{13} = -\frac{\varepsilon_{22}}{\varepsilon_{11}} \ , \ v_{23} = -\frac{\varepsilon_{33}}{\varepsilon_{22}}$$

The in-plane shear modulus can be determined from a specimen positioned at ± 45° by employing the subsequent equation.

$$G_{12} = \frac{E_{11}}{2(1 + v_{12})}$$

(21)

When it comes to polymers, the substance is recognized for displaying anisotropic characteristics, and the stress-strain response can be articulated in Cartesian coordinates as stated in [45]:

$$\varepsilon_{11} = \frac{1}{E}\left[\sigma_{11} v(\sigma_{22} + \sigma_{33}) \right] + \alpha_e \Delta T$$

$$\varepsilon_{22} = \frac{1}{E}\left[\sigma_{22} v(\sigma_{11} + \sigma_{33}) \right] + \alpha_e \Delta T$$

$$\varepsilon_{33} = \frac{1}{E}\left[\sigma_{33} v(\sigma_{11} + \sigma_{22}) \right] + \alpha_e \Delta T$$

$$\varepsilon_{xy} = \frac{1+v}{E}\sigma_{xy} \ , \ \varepsilon_{xz} = \frac{1+v}{E}\sigma_{xz} \ , \ \varepsilon_{yz} = \frac{1+v}{E}\sigma_{yz}$$

(22)

where α_ε is the coefficient of thermal expansion. The thermal deformation can be determined as follows:

$$\varepsilon_{th} = \alpha_e \Delta T$$

(23)

The effective stress σ_{eff} and von Mises stress σ_{Mises} can be calculated as follows:

$$\sigma_{eff} = \sqrt{\sigma_{11}{}^2 + \sigma_{22}{}^2 + \sigma_{33}{}^2 + 2v(\sigma_{11}\sigma_{22} + \sigma_{11}\sigma_{33} + \sigma_{22}\sigma_{33})}$$

$$\sigma_{Mises} = \sqrt{\frac{1}{2}\left[(\sigma_{11}{}^2 - \sigma_{22}{}^2)^2 + (\sigma_{22}{}^2 - \sigma_{33}{}^2)^2 + (\sigma_{33}{}^2 - \sigma_{11}{}^2)^2 \right]}$$

(24)

b. Thermal Analysis

Thermomechanical analysis involves a sequential coupling of stress analysis and heat, establishing an indirect connection. In the numerical representation, the inclusion of heat transfer enables the computation of temperature fluctuations during the printing procedure. The governing partial differential equation governing heat transfer is articulated as follows:

$$\rho C_p \frac{\partial T}{\partial t} = k\left(\frac{\partial^2 T}{\partial x^2} + \frac{\partial^2 T}{\partial y^2} + \frac{\partial^2 T}{\partial z^2} \right)$$

(25)

in which k (in W/m·K), C_p (in J/kg·K) and ρ (in kg/m³)

express the thermal conductivity, specific heat capacity and the density of the polymer, respectively. The thermal energy H linked to the solidification of the phase is estimated in the following manner:

$$H = \int \rho C_p(T)dT$$

(26)

The layers in print were placed in the thickness orientation. A fresh layer, added at temperature T_m, undergoes cooling to match the chamber temperature T_c. Throughout the printing procedure, the layers experience heating through conduction, causing their temperature to surpass T_g. The thickness of the component is built up in the z-direction, maintaining a consistent chamber temperature T_c. In this dimension, the temporal evolution of temperature, denoted as $T(z,t)$, adheres to the subsequent thermal equation during time t:

$$\rho C_p \frac{\partial T}{\partial t} = k \frac{\partial^2 T}{\partial z^2}$$

(27)

The solution to this equation is as follows [46]:

$$T(z,t) = T_c + \frac{H}{\rho C_p} \frac{1}{\sqrt{\pi \kappa t}} \exp\left(-\frac{z^2}{4\kappa t}\right)$$

(28)

When κ is defined as $k/\rho \cdot C_p$, representing the thermal diffusivity of the polymer in (m^2/s), and the printed component possesses considerable dimensions, particularly with a thickness e that surpasses the layer thickness Δe, the thermal energy of the layer can be acquired [47]:

$$H = \rho C_p \Delta e (T_m - T_c)$$

(29)

The method to acquire the temperature fluctuation across the thickness of the component is as follows:

$$T(z,t) = T_c + (T_m - T_c)\frac{\Delta e}{\sqrt{\pi \kappa t}} \exp\left(-\frac{z^2}{4\kappa t}\right)$$

(30)

where the initial state temperature is $T(z,t=0)=23℃$. Equation (30) allows for the calculation of the temperature variation at the position z. For instance, to define the layer at which the temperature T is equal to T_g at a given time t during the printing process, one writes:

$$z(t) = 2\sqrt{\kappa t}\sqrt{\ln\left(\frac{\Delta e}{\sqrt{\pi \kappa}}\frac{T_m - T_c}{T_g - T_c}\right) - \ln\sqrt{t}}$$

(31)

This equation applies to the printing characteristics of materials. The resilience and dimensional consistency of printed components are influenced by residual stresses and warping introduced during the process. Wang et al. [48] formulated a straightforward analytical model, employing thorough simplifications, to forecast warping deformation following the FFF (Fused Filament Fabrication) procedure in ABS. They quantitatively scrutinized all contributing factors and obtained the subsequent expression for forecasting inter-layer warping δ_T:

$$\delta_T = \frac{3}{4}\alpha_e(T_v - T_c)\frac{L_i^2 \Delta e}{e^2}\left(1 - \frac{\Delta e}{e}\right)$$

(32)

where L_i represents the section length of the part, and $n=e/\Delta e$ represents the number of deposited layers. Derived from the examination of the model, some recommendations have been made to effectively reduce warping phenomena. According to this simple analytical model [47], the amount of deformation increases more than linearly with L_i, is proportional to the layer thickness Δe, and decreases monotonically with the increase in thickness e, meaning that warping is pronounced in the thin sections of the part. Additionally, the degree of deformation δ_T of the layer depends on the temperature gradient $(T_g - T_c)$, as well as the coefficient of thermal expansion α_e, In accordance with the association outlined in Equation (32).

ii. FFF process parameters

The performing hydrofoil profile NTS1020 is used to 3D print the blade using the FFF method [49]. FFF technology involves melting and extruding a polymer material filament to layer by layer print a part. The fiber aspect ratio is 10, and the reinforcements have a tensor with random orientation (a_{11}=0.33, a_{22}=0.33, a_{33}=0.33). The printer nozzle has multiple orientations during printing, but short fibers in the polymer tend to align with the printing direction [50]. Hence, the polymer's average fiber orientation is deemed to be random. In order to fabricate a component, the G-code must be derived from the geometric file in *.stl format. The G-code, produced by the Ultimaker 3 slicer software, includes directives for movement, extrusion, and heating. These commands are interpreted by the

printer to create a 3D model. The Digimat-AM requires a toolpath based on the G-code, and the voxel method is utilized to mesh the blade. Following this, finite element analysis is employed to extract data related to residual stresses, temperature, and deformation fields in the modified blade.

3. Results and Discussion

The selection of the appropriate 3D printing technique depends on the specific requirements of your project and the allocated budget [51]. In the context of FFF printers, the resolution is contingent upon the nozzle size and the precision of extruder movements. Various factors, such as deformation, layer misalignment, shifting, and lower part shrinkage, contribute to decreased precision and surface smoothness of printed components. In contrast, SLS printers consistently yield objects with superior resolution compared to FFF printers, primarily determined by the optical spot size of the laser. Moreover, SLS printing exerts less force on the model, resulting in a much smoother surface finish. Additionally, the SLS method enables the production of intricate parts in a single process without requiring glue, unlike the FFF method, as powders function as a supportive structure for the printed components.

The Fused Filament Fabrication (FFF) technique is a prevalent technology in the consumer 3D printing sector due to its comparatively affordable nature. However, it comes with inherent technical limitations. In contrast, Selective Laser Sintering (SLS) printers are typically utilized in professional or industrial settings due to the higher cost of the machines. This cost is justified by the superior quality and technical capabilities of the printed components. Unlike the FFF method, the SLS approach doesn't necessitate structural support during printing, leading to shorter printing times. Post-processing for SLS-printed objects is less intricate compared to other technologies. It involves the removal of unused or unfused powder that acts as support during printing. This task can be carried out manually or with the use of compressed air. On the other hand, post-processing for FFF presents challenges. Inadequate dissolution of the support structure can potentially harm the print or result in surface imperfections. Moreover, specialized equipment such as glass containers or an ultrasonic bath is required [52].

The bonding strength between layers in SLS printing is very strong. This means that parts printed by SLS have almost isotropic mechanical properties. In FFF, printed objects are weaker in the vertical construction direction due to the anisotropy of material properties resulting from the additive layering method. FFF objects are anisotropic, and when weight is applied, these printed objects can be damaged if not oriented correctly. In short, FFF parts do not have the same strength in all directions, emphasizing the importance of orientation in the design and printing of robust parts.

Warping is a prevalent issue in the manufacturing process. As the material undergoes solidification through the FFF technique, a reduction in its dimensions occurs due to the cooling process. Since various segments of the printed object experience distinct cooling rates, their dimensions also alter unevenly. This non-uniform cooling results in the development of internal stresses, which subsequently cause the lower layer to be pulled upward, leading to warping. Similar to FFF, SLS objects are also prone to warping and shrinkage. The thermoplastic powder must be subjected to high temperatures for sintering, meaning the printed object undergoes a cooling process almost immediately after the formation of the solid layer. As the printed part cools, it contracts and shrinks in all directions, potentially resulting in imprecise dimensions. Stress due to contraction can also accumulate in certain parts of the printed piece, especially in corners and sharp edges, leading to warping or deformation of these areas.

Figure 11 presents a comparison during the printing and cooling processes between the SLS and FFF additive manufacturing methods of the printed blade based on mechanical deflection, residual stress, and warping. These thermomechanical properties were evaluated based on the volume fraction of carbon (CB) and glass (GB) particles with the PA12 polymer. According to the simulation results discussed earlier for both printing methods, a general conclusion can be drawn that increasing the volume fraction of particles increases von Mises residual stress, leading to a decrease in the mechanical deflection and warping observed in the printed component. Also, the mechanical response of the FFF-printed blade during printing is much more significant than that with SLS printing for mechanical deflection and von Mises residual stress (Figure 11) due to the high printing speed and significant mechanical forces demonstrated by the FFF method. However, the opposite is observed for the mechanical warping of the PA12-CB/GB-based blade, where it is more significant for the SLS method than for the FFF method (Figure 12). The addition of CB/GB particles can generate a uniform cooling rate throughout the blade, and the shrinkage of the blade becomes uniform, reducing

warping, and indicating the dominant effect of these particles in resisting sample shrinkage. As the volume fraction of CB/GB particles increases, the coefficient of thermal expansion (CTE) decreases, resulting in low mechanical warping of the blade, due to the proportional relationship between the CTE and warping as shown in equation 32.

It is observed in Figure 11 that the mechanical deflection of the printed blade decreases with increasing volume fraction due to the improvement in mechanical stiffness. However, residual stress increases with volume fraction due to the accumulation of temperature gradient during printing. On the other hand, the temperature of the blade at the final printing stage increases slightly, due to the improvement in the thermal capacity of the polymer by adding the particles. Thus, by using the particles, the coefficient of thermal expansion decreases, which reduces mechanical warpage. In addition, the deflection and residual stress have higher values during cooling than during printing. This is because the accumulated temperature gradient generates residual stress during printing, and when the blade cools, the temperature gradient decreases and mechanical shrinkage becomes significant, resulting in high deflection and high residual stress compared to printing.

The vol% refers to the volume fraction of carbon/glass particles. The effect of vol% on the results of this study is significant as it directly impacts the mechanical properties and performance of the composite material. A higher vol% typically leads to increased reinforcement within the composite, resulting in enhanced strength, stiffness, and other mechanical properties. The study likely explores various volume fractions to assess how they influence the structural integrity, durability, and overall performance of the 3D printed composite material, providing insights into the most suitable reinforcement content for optimal turbine blade construction.

Mechanical warping is connected to the temperature field experienced by the material during printing, and since PA12 undergoes a higher temperature during SLS printing than FFF printing [53], warping is more pronounced in SLS. The combination of the high temperature in the SLS build chamber and the additional heating due to the laser results in significant degradation of the entire PA12 material. Numerous investigations have demonstrated that the characteristics of PA12 degrade when subjected to elevated temperatures over prolonged durations. Polymer chain crosslinking leads to an increase in molecular weight, which raises the viscosity in the molten state of the material and decreases its yield strength and elongation at break [54].

The deformation of parts in FFF printing is attributed to the quick heating and cooling cycles of the feedstock material, resulting in the accumulation of residual stresses during part construction. Previous findings suggest that composites with low residual stresses tend to exhibit more warping, and conversely, those with higher residual stresses experience less warping. Consequently, the FFF process shows higher residual stress, as depicted in Figure 11, leading to reduced warping, as illustrated in Figure 12. To elaborate, FFF has a higher printing speed, and it is evident that shrinkage increases with the acceleration of printing speed across all composite materials. This indicates that residual stress escalates with printing speed [55]. In contrast, in SLS, the printing speed is lower compared to FFF, resulting in heightened mechanical warping of the printed blade in the case of SLS.

Shrinkage is described as a modification in dimensions, while warping is characterized by alterations in shape. The primary factor contributing to warping is the inconsistency in shrinkage. When a component uniformly contracts in all dimensions, it diminishes in size while maintaining its original form. Conversely, if specific elements of the component experience disparate rates of shrinkage, it gives rise to internal stresses. Should these stresses surpass the structural rigidity, deformation, known as warping, occurs in the object.

The tidal turbine blade can be subjected to extreme forces in the marine environment. The direction of the force $\vec{F}$ is probably vertical to the blade, representing the flow of marine currents. We depict two illustrative diagrams in Figure 13 showing mechanical delamination, which is low for the SLS method due to the high bonding strength between layers. In contrast, for the FFF method with weak bonds, the blade can quickly incur damage through delamination under vertical printing forces.

It can be concluded that it is better to print the blade using the SLS method despite the significant warping observed, which can be compensated for. The harsh nature of the marine environment where the hydrofoil blade is located imposes isotropic loads in all directions that the blade may experience, eventually leading to its damage. It is deduced that the FFF method should be avoided in the construction of these structures, despite its low mechanical warping, due to the anisotropic property of this method.
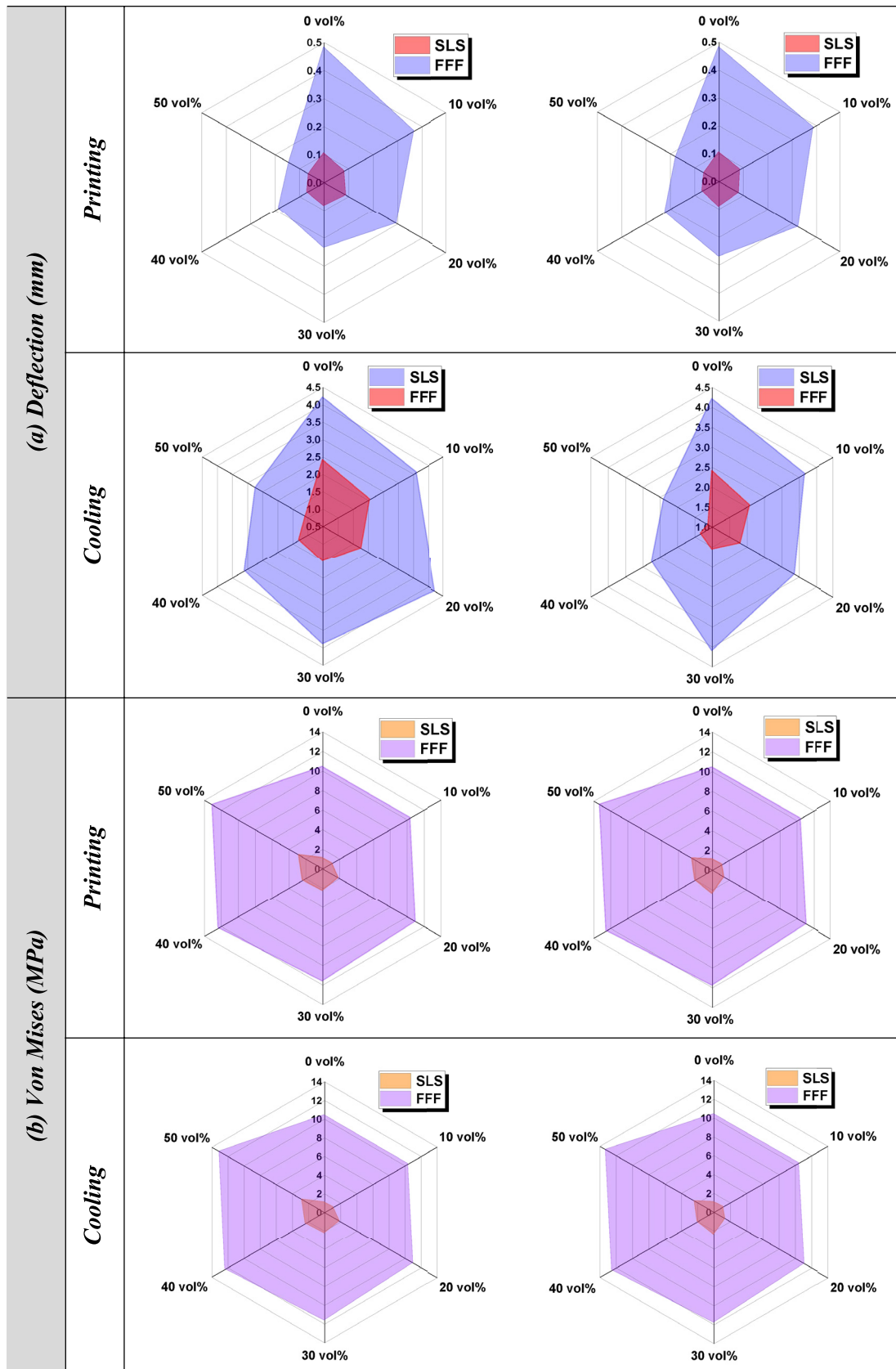
Figure 11. Comparison between the thermomechanical properties of the blade printed with PA12-CB/GB using SLS and FFF. Mechanical deflection (a) and von Mises residual stress (b).
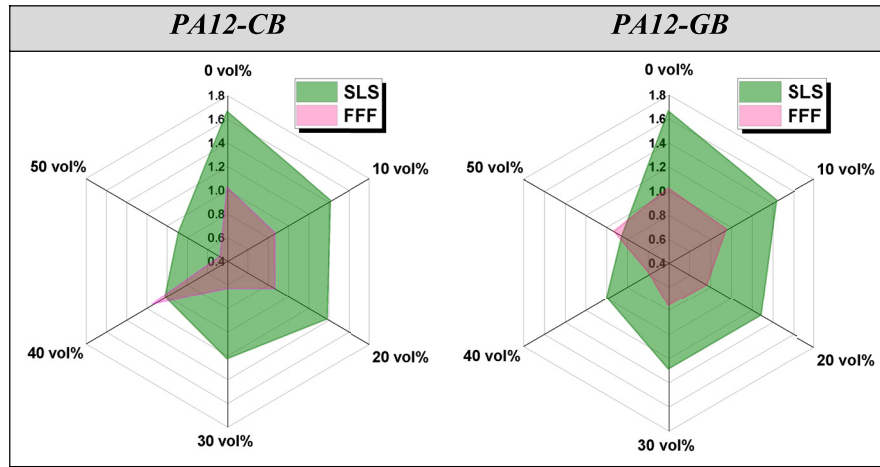
Figure 12. Comparison between the mechanical warping of the blade printed with PA12-CB/GB using SLS and FFF.
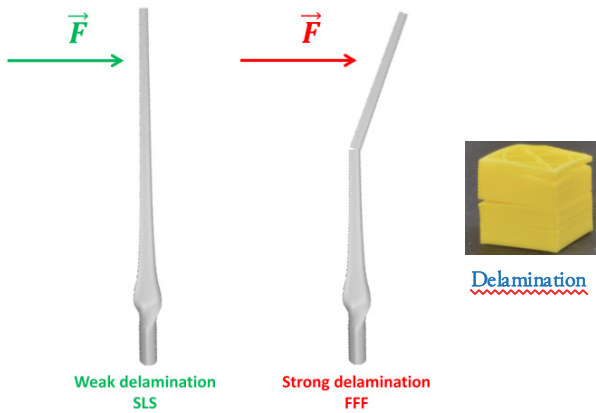

Figure 13. Comparison between the mechanical delamination of the blade printed with SLS and FFF.

4. Conclusions

The study delved into the thermomechanical characteristics of a hydrofoil blade produced through 3D printing. The utilized material is a thermoplastic polymer enriched with carbon and glass beads (CB/GB). Findings indicate that the deflection pattern undergoes changes with distinct printing materials. Additionally, an analysis is conducted to explore the impact of polymer reinforcement on mechanical strength concerning deformation and residual stress. Computational findings highlight the notable mechanical strength of reinforced polymers in comparison to their unreinforced counterparts. Furthermore, this reinforcement proves valuable in mitigating mechanical warping.

Furthermore, it can be inferred that the compact blade can be rapidly manufactured using economical FFF printers. The 3D printing procedure involves several phases and enhancements to achieve peak performance after numerous simulations. The thermomechanical effects were examined using improved thermoplastic materials. Simulation results revealed that the PA12-CB/GB printed blade displayed outstanding mechanical performance, characterized by minimal deflection and mechanical warping. Furthermore, a comparative analysis of two printing methods, SLS and FFF, was conducted. It was determined that employing the SLS method for blade printing is preferable due to the blade's isotropic properties, despite notable warping that can be rectified with particles. The marine environment, where the hydrofoil blade is situated, is known for its harsh conditions. The FFF-printed blade exhibits anisotropic properties, which are undesirable for these structures, despite having low mechanical warping. In conclusion, this numerical analysis offers optimization insights for hydrofoil design and demonstrates promise in printing compact blades. However, further research is necessary to advance additive manufacturing for the benefit of renewable energy applications.

Author Contributions

Marwane Rouway: investigation, methodology, and data curation, **Mourad Nachtane**: writing, reviewing, and original draft preparation. **Mostapha Tarfaoui**: supervision, writing, and validation. **S. Jamoudi Sbai**: data collection, conceptualization, and editing.

Funding

Acknowledgments

We would like to express our sincere appreciation to ENSTA Bretagne for generously providing the essential software tools and advanced 3D printing equipment that greatly enhanced the success of this research paper.

Conflict of Interest

There is no conflict of interest.

References

[1] Tarfaoui, M., Nachtane, M., Amry, Y., et al., 2018. From renewable to marine energies sources for sustainable development and energy transition in Morocco: Current status and scenario. Preprints. DOI: https://doi.org/10.20944/preprints201811.0568.v1

[2] Mourad, N., Mostapha, T., Dennoun, S., et al. (editors), 2018. Promotion of renewable marines energies in Morocco: Perspectives and strategies. 20th International Conference on Energy Management and Renewable Energy; 2018 Jan; Dubai, UAE.

[3] Nachtane, M., Tarfaoui, M., Saifaoui, D., et al., 2018. Evaluation of durability of composite materials applied to renewable marine energy: Case of ducted tidal turbine. Energy Reports. 4, 31–40.
DOI: https://doi.org/10.1016/j.egyr.2018.01.002

[4] Nachtane, M., 2019. Marine renewable energies and study of the performance of composite materials: case of a tidal current turbine [Ph.D. thesis]. Rennes: Loire Bretagne University. (in French).

[5] Nachtane, M., Tarfaoui, M., Goda, I., et al., 2020. A review on the technologies, design considerations and numerical models of tidal current turbines. Renewable Energy. 157, 1274–1288.
DOI: https://doi.org/10.1016/j.renene.2020.04.155

[6] Nachtane, M., Tarfaoui, M., Mohammed, M.A., et al., 2020. Effects of environmental exposure on the mechanical properties of composite tidal current turbine. Renewable Energy. 156, 1132–1145.
DOI: https://doi.org/10.1016/j.renene.2020.04.126

[7] Nachtane, M., Tarfaoui, M., Saifaoui, D., et al., 2020. Hydrodynamic performance evaluation of a new hydrofoil design for marine current turbines. Materials Today: Proceedings. 30, 889–898.
DOI: https://doi.org/10.1016/j.matpr.2020.04.346

[8] Tarfaoui, M., Nachtane, M., Goda, I., et al., 2020. 3D printing to support the shortage in personal protective equipment caused by COVID-19 pandemic. Materials. 13(15), 3339.
DOI: https://doi.org/10.3390/ma13153339

[9] El Moumen, A., Tarfaoui, M., Lafdi, K., 2019. Modelling of the temperature and residual stress fields during 3D printing of polymer composites. The International Journal of Advanced Manufacturing Technology. 104, 1661–1676.
DOI: https://doi.org/10.1007/s00170-019-03965-y

[10] Tarfaoui, M., Qureshi, Y., Chihi, M., et al., 2023. Mechanical characterisation of Aerosil-polycarbonate-based ceramic nanocomposites: 3D printing versus injection moulding technology. Journal of Composite Materials. 57(29), 4615–4634.
DOI: https://doi.org/10.1177/00219983231214556

[11] Daly, M., Tarfaoui, M., Chihi, M., et al., 2023. FDM technology and the effect of printing parameters on the tensile strength of ABS parts. The International Journal of Advanced Manufacturing Technology. 126, 5307–5323.
DOI: https://doi.org/10.1007/s00170-023-11486-y

[12] Nachtane, M., Tarfaoui, M., Ledoux, Y., et al., 2020. Experimental investigation on the dynamic behavior of 3D printed CF-PEKK composite under cyclic uniaxial compression. Composite Structures. 247, 112474.
DOI: https://doi.org/10.1016/j.compstruct.2020.112474

[13] Rouway, M., Nachtane, M., Tarfaoui, M., et al., 2021. 3D printing: Rapid manufacturing of a new small-scale tidal turbine blade. The International Journal of Advanced Manufacturing Technology. 115, 61–76.
DOI: https://doi.org/10.1007/s00170-021-07163-7

[14] Rouway, M., Tarfaoui, M., Chakhchaoui, N., et al., 2023. Additive manufacturing and composite materials for marine energy: Case of tidal turbine. 3D Printing and Additive Manufacturing. 10(6), 1309–1319.
DOI: https://doi.org/10.1089/3dp.2021.0194

[15] Shchegolkov, A.V., Nachtane, M., Stanishevskiy, Y.M., et al., 2022. The effect of multi-walled carbon nanotubes on the heat-release properties

of elastic nanocomposites. Journal of Composites Science. 6(11), 333.
DOI: https://doi.org/10.3390/jcs6110333

[16] El Bahi, A., Rouway, M., Tarfaoui, M., et al., 2023. Mechanical homogenization of transversely isotropic CNT/GNP reinforced biocomposite for wind turbine blades: Numerical and analytical study. Journal of Composites Science. 7(1), 29.
DOI: https://doi.org/10.3390/jcs7010029

[17] Beloufa, H.I., Tarfaoui, M., Lafdi, K., et al., 2023. Graphene nanosheets as novel nanofillers in an epoxy matrix for improved mechanical properties. Advances in nanosheets—Preparation, properties and applications. IntechOpen: London.

[18] Rouway, M., Nachtane, M., Tarfaoui, M., et al., 2021. Mechanical properties of a biocomposite based on carbon nanotube and graphene nanoplatelet reinforced polymers: Analytical and numerical study. Journal of Composites Science. 5(9), 234.
DOI: https://doi.org/10.3390/jcs5090234

[19] Momeni, F., Sabzpoushan, S., Valizadeh, R., et al., 2019. Plant leaf-mimetic smart wind turbine blades by 4D printing. Renewable Energy. 130, 329–351.
DOI: https://doi.org/10.1016/j.renene.2018.05.095

[20] Galvez, G.M., Olivar, K.A.M., Tolentino, F.R.G., et al., 2022. Finite element analysis of different infill patterns for 3D printed tidal turbine blade. Sustainability. 15(1), 713.
DOI: https://doi.org/10.3390/su15010713

[21] Ramírez-Elías, V.A., Damian-Escoto, N., Choo, K., et al., 2022. Structural analysis of carbon fiber 3D-printed ribs for small wind turbine blades. Polymers. 14(22), 4925.
DOI: https://doi.org/10.3390/polym14224925

[22] Arivalagan, S., Sappani, R., Čep, R., et al., 2023. Optimization and experimental investigation of 3D printed micro wind turbine blade made of PLA material. Materials. 16(6), 2508.
DOI: https://doi.org/10.3390/ma16062508

[23] Wang, B., Ming, Y., Zhu, Y., et al., 2020. Fabrication of continuous carbon fiber mesh for lightning protection of large-scale wind-turbine blade by electron beam cured printing. Additive Manufacturing. 31, 100967.
DOI: https://doi.org/10.1016/j.addma.2019.100967

[24] Ming, Y., Duan, Y., Zhang, S., et al., 2020. Self-heating 3D printed continuous carbon fiber/epoxy mesh and its application in wind turbine deicing. Polymer Testing. 82, 106309.
DOI: https://doi.org/10.1016/j.polymertesting.2019.106309

[25] Kim, S.I., Jung, H.Y., Yang, S., et al., 2022. 3D Printing of a miniature turbine blade model with an embedded fibre Bragg grating sensor for high-temperature monitoring. Virtual and Physical Prototyping. 17(2), 156–169.
DOI: https://doi.org/10.1080/17452759.2021.2017545

[26] Nachtane, M., Meraghni, F., Chatzigeorgiou, G., et al., 2022. Multiscale viscoplastic modeling of recycled glass fiber-reinforced thermoplastic composites: Experimental and numerical investigations. Composites Part B: Engineering. 242, 110087.
DOI: https://doi.org/10.1016/j.compositesb.2022.110087

[27] Rahimizadeh, A., Kalman, J., Fayazbakhsh, K., et al., 2021. Mechanical and thermal study of 3D printing composite filaments from wind turbine waste. Polymer Composites. 42(5), 2305–2316.
DOI: https://doi.org/10.1002/pc.25978

[28] Rahimizadeh, A., Kalman, J., Fayazbakhsh, K., et al., 2019. Recycling of fiberglass wind turbine blades into reinforced filaments for use in Additive Manufacturing. Composites Part B: Engineering. 175, 107101.
DOI: https://doi.org/10.1016/j.compositesb.2019.107101

[29] Tahir, M., Rahimizadeh, A., Kalman, J., et al., 2021. Experimental and analytical investigation of 3D printed specimens reinforced by different forms of recyclates from wind turbine waste. Polymer Composites. 42(9), 4533–4548.
DOI: https://doi.org/10.1002/pc.26166

[30] Jha, D., Singh, M., Thakur, A.N., 2021. A novel computational approach for design and performance investigation of small wind turbine blade with extended BEM theory. International Journal of Energy and Environmental Engineering. 12, 563–575.
DOI: https://doi.org/10.1007/s40095-021-00388-y

[31] Leong, K.F., Liu, D., Chua, C.K., 2014. Tissue engineering applications of additive manufacturing. Comprehensive materials processing. Elsevier: Oxford.

[32] Yang, L., Hsu, K., Baughman, B., et al., 2017. Additive manufacturing of metals: The technology, materials, design and production. Springer International Publishing: Cham.

[33] Study of Laser Microprinting of Biological Elements for Bone Tissue Engineering [Internet] [cited 2020 Apr 8]. Available from: http://www.theses.fr/2010BOR14108 (in French).

[34] Sturm, L.D., Williams, C.B., Camelio, J.A., et al., 2017. Cyber-physical vulnerabilities in additive manufacturing systems: A case study attack on the .STL file with human subjects. Journal of Manufacturing Systems. 44, 154–164.
DOI: https://doi.org/10.1016/j.jmsy.2017.05.007

[35] Shanthar, R., Chen, K., Abeykoon, C., 2023. Powder-based additive manufacturing: A critical review of materials, methods, opportunities, and challenges. Advanced Engineering Materials. 25(19), 2300375.
DOI: https://doi.org/10.1002/adem.202300375

[36] Kim, D., Oh, S., 2018. Optimizing the design of a vertical ground heat exchanger: measurement of the thermal properties of bentonite-based grout and numerical analysis. Sustainability. 10(8), 2664.
DOI: https://doi.org/10.3390/su10082664

[37] Jacobs, P.F., 1992. Rapid prototyping & manufacturing: Fundamentals of stereolithography. Society of Manufacturing Engineers: Southfield.

[38] Dong, L., Makradi, A., Ahzi, S., et al., 2007. Finite element analysis of temperature and density distributions in selective laser sintering process. Materials science forum. Trans Tech Publications Ltd.: Bäch. pp. 75–80.

[39] Tekinalp, H.L., Kunc, V., Velez-Garcia, G.M., et al., 2014. Highly oriented carbon fiber-polymer composites via additive manufacturing. Composites Science and Technology. 105, 144–150.
DOI: https://doi.org/10.1016/j.compscitech.2014.10.009

[40] Shofner, M.L., Lozano, K., Rodríguez-Macías, F.J., et al., 2003. Nanofiber-reinforced polymers prepared by fused deposition modeling. Journal of Applied Polymer Science. 89(11), 3081–3090.
DOI: https://doi.org/10.1002/app.12496

[41] Zawaski, C., Williams, C., 2020. Design of a low-cost, high-temperature inverted build environment to enable desktop-scale additive manufacturing of performance polymers. Additive Manufacturing. 33, 101111.
DOI: https://doi.org/10.1016/j.addma.2020.101111

[42] Li, Y., Zhou, K., Tan, P., et al., 2018. Modeling temperature and residual stress fields in selective laser melting. International Journal of Mechanical Sciences. 136, 24–35.
DOI: https://doi.org/10.1016/j.ijmecsci.2017.12.001

[43] Bähr, F., Westkämper, E., 2018. Correlations between influencing parameters and quality properties of components produced by fused deposition modeling. Procedia CIRP. 72, 1214–1219.
DOI: https://doi.org/10.1016/j.procir.2018.03.048

[44] Christiyan, K.G.J., Chandrasekhar, U., Venkateswarlu, K., 2016. A study on the influence of process parameters on the Mechanical Properties of 3D printed ABS composite. IOP Conference Series: Materials Science and Engineering. 114(1), 012109.
DOI: https://doi.org/10.1088/1757-899X/114/1/012109

[45] Yilbas, B.S., Arif, A.F.M., 2001. Material response to thermal loading due to short pulse laser heating. International Journal of Heat and Mass Transfer. 44(20), 3787–3798.
DOI: https://doi.org/10.1016/S0017-9310(01)00026-6

[46] Carslaw, H.S., Jaeger, J.C., 1959. Conduction of heat in solids. Clarendon Press: Oxford.

[47] Armillotta, A., Bellotti, M., Cavallaro, M., 2018. Warpage of FDM parts: Experimental tests and analytic model. Robotics and Computer-Integrated Manufacturing. 50, 140–152.
DOI: https://doi.org/10.1016/j.rcim.2017.09.007

[48] Wang, T.M., Xi, J.T., Jin, Y., 2007. A model research for prototype warp deformation in the FDM process. The International Journal of Advanced Manufacturing Technology. 33, 1087–1096.
DOI: https://doi.org/10.1007/s00170-006-0556-9

[49] Nachtane, M., Tarfaoui, M., Saifaoui, D., et al., 2020. Hydrodynamic performance evaluation of a new hydrofoil design for marine current turbines. Materials Today: Proceedings. 30, 889–898.
DOI: https://doi.org/10.1016/j.matpr.2020.04.346

[50] Ferreira, R.T.L., Amatte, I.C., Dutra, T.A., et al., 2017. Experimental characterization and micrography of 3D printed PLA and PLA reinforced with short carbon fibers. Composites Part B: Engineering. 124, 88–100.
DOI: https://doi.org/10.1016/j.compositesb.2017.05.013

[51] Msallem, B., Sharma, N., Cao, S., et al., 2020. Evaluation of the dimensional accuracy of 3D-printed anatomical mandibular models using

FFF, SLA, SLS, MJ, and BJ printing technology. Journal of Clinical Medicine. 9(3), 817. DOI: https://doi.org/10.3390/jcm9030817

[52] Tully, J.J., Meloni, G.N., 2020. A scientist's guide to buying a 3D printer: How to choose the right printer for your laboratory. Analytical Chemistry. 92(22), 14853–14860. DOI: https://doi.org/10.1021/acs.analchem. 0c03299

[53] A. Lifton, V., Lifton, G., Simon, S., 2014. Options for additive rapid prototyping methods (3D printing) in MEMS technology. Rapid Prototyping Journal. 20(5), 403–412.

DOI: https://doi.org/10.1108/RPJ-04-2013-0038

[54] Mwania, F.M., Maringa, M., van der Walt, J.G., 2022. Investigating the recyclability of laser PP CP 75 polypropylene powder in laser powder bed fusion (L-PBF). Polymers. 14(5), 1011. DOI: https://doi.org/10.3390/polym14051011

[55] Zhang, W., Wu, A.S., Sun, J., et al., 2017. Characterization of residual stress and deformation in additively manufactured ABS polymer and composite specimens. Composites Science and Technology. 150, 102–110. DOI: https://doi.org/10.1016/j.compscitech. 2017.07.017